



HAL
open science

Using a physics constrained U-Net for real-time compatible extraction of physical features from WEST divertor hot-spots

Valentin Gorse, Raphaël Mitteau, Julien Marot

► **To cite this version:**

Valentin Gorse, Raphaël Mitteau, Julien Marot. Using a physics constrained U-Net for real-time compatible extraction of physical features from WEST divertor hot-spots. *Journal of Fusion Energy*, 2024, 43, pp.13. 10.1007/s10894-024-00405-y . cea-04828988

HAL Id: cea-04828988

<https://cea.hal.science/cea-04828988v1>

Submitted on 10 Dec 2024

HAL is a multi-disciplinary open access archive for the deposit and dissemination of scientific research documents, whether they are published or not. The documents may come from teaching and research institutions in France or abroad, or from public or private research centers.

L'archive ouverte pluridisciplinaire **HAL**, est destinée au dépôt et à la diffusion de documents scientifiques de niveau recherche, publiés ou non, émanant des établissements d'enseignement et de recherche français ou étrangers, des laboratoires publics ou privés.



Using a Physics Constrained U-Net for Real-Time Compatible Extraction of Physical Features from WEST Divertor Hot-Spots

Valentin Gorse¹ · Raphaël Mitteau¹ · Julien Marot² · the WEST TEAM¹

Accepted: 11 April 2024 / Published online: 13 May 2024

© The Author(s), under exclusive licence to Springer Science+Business Media, LLC, part of Springer Nature 2024

Abstract

The WEST (W Environment in Steady-state Tokamak) divertor serves as the primary element for heat exhaust and contributes critically to plasma control. The divertor receives intense heat fluxes, potentially leading to damage to the plasma facing units. Hence, it is of major interest for the safety of divertor operation to detect and characterize the hot spots appearing on the divertor surface. This is done through the use of infrared (IR) cameras, which provide a thermal mapping of the divertor surface. In this work, a knowledge-informed divertor hot spot detector is demonstrated, that explicitly accounts for hot spot structure and temperature repartition. A novel neural network, termed as Constrained U-Net, is proposed, which uses as input the bounding boxes of hot spots from prior automatic detection. The Constrained U-Net addresses jointly image segmentation and regression of physical parameters, while remaining compatible with the practical constraints of real-time use. The detector is trained on simulated data and applied to real-world infrared images. On simulated images, it yields a precision of 0.98, outperforming a classical U-Net, and Max-Tree. Visual results obtained on real-world acquisitions from the WEST Tokamak illustrate the reliability of the proposed method for safety studies on hot spots.

Keywords Nuclear fusion · Deep learning · WEST Tokamak · Divertor · Hot spots · Constrained U-Net · Infrared videos · Physical features

Introduction

The pursuit of harnessing fusion energy has led to the development of Tokamak fusion plasmas, which fuse Deuterium (D) and Tritium (T) atoms. This process holds immense promise as a future energy source. The power capabilities of Tokamaks have been steadily increasing, with the JET Tokamak achieving fusion outputs between 5 and 20 MW [1] and the International Thermonuclear Experimental Reactor (ITER) projected to reach up to 500 MW [2].

Magnetic fusion devices are trending towards continuous plasma operation, lasting several minutes, resulting in energy throughputs comparable to significant power plants. For example, the W Environment in Steady-state Tokamak (WEST) [3] routinely operates with 4 MW of power for a plasma duration exceeding a minute.

The substantial power and energy involved are dissipated through the walls, which function as thermal shields. These walls operate in a stationary manner with surface temperatures ranging from 500 to 1000 °C. In addition to regular power evacuation, which must be monitored, parasitic phenomena such as magnetic instabilities and additional heating power losses direct occasionally hot plasma to undesirable locations. This can result in potentially damaging thermal events, as the plasma discharge duration extends and surpasses the thermal stabilization time. Monitoring and counter-reaction are tools for optimal machine operation, and are becoming increasingly prevalent among tokamaks/fusion machines.

As the plasma discharge duration extends and surpasses the thermal stabilization time, active temperature control of Plasma facing components during plasma operation is

✉ Valentin Gorse
valentin.gorse@cea.fr

Raphaël Mitteau
raphael.mitteau@cea.fr

Julien Marot
julien.marot@fresnel.fr

¹ IRFM CEA Cadarache, 13108 Saint-Paul-Lez-Durance, France

² Aix-Marseille Université, CNRS, Centrale Méditerranée, Institut Fresnel, 13013 Marseille, France

becoming increasingly prevalent among tokamaks/fusion machines.

Relation to Prior Work in the Field

Active temperature feedback control is implemented in various tokamaks and can be based on several types of input data. Several research groups associated with the Experimental Advanced Superconducting Tokamak (EAST) are currently engaged in the task of plasma-wall divertor control. This endeavor involves the utilization of a multitude of instrument measurements [4].

Analog CCD cameras operating in the near infrared wavelength are used to measure surface temperature of the plasma facing components in JET Tokamak [5].

Numerous tokamak facilities have opted to incorporate infrared diagnostics for real-time surveillance. This strategic decision is also aimed at preparing for the forthcoming operation of ITER, which will similarly rely on infrared diagnostics. Different research teams from all over the world such as the WEST tokamak in southern France, EAST tokamak in China [6], or Wendelstein 7-X (W7-X) stellarator in Germany [7] are working on automating infrared (IR) image analysis to address machine safety concerns.

Regarding the use of this diverse input data, a broad spectrum of methods for real-time control is developed. For instance, certain teams implement fixed thresholds on infrared images to provide feedback on plasma conditions [8]. Neural networks have been a naturally explored method for plasma control since the early 1990s [9]. Within this category of neural networks, their application is diverse. A recent example is the reinforcement learning method tested on the Swiss TCV tokamak [10]. Use of neural network methodologies for computing heat fluxes deposition on W7-X divertor have been demonstrated [11, 12]. These applications, while yielding encouraging outcomes, also pave the way for potential real-time implementations. This signifies a substantial advancement in the field. The work presented in this article is a part of the application of neural networks on the infrared images of the WEST tokamak, as described in [13].

Main Contribution

The control of the plasma-wall interaction in the divertor presents a significant challenge due to the difficulty of detecting and analysing all hot spots. On the divertor, most of these hot spots are the so-called "strikelines", which are the main contact point for the plasma to the divertor. The automatic detection of a region of interest (ROI) that contains a single strikeline is considered state-of-the-art. The focus is here placed on the analysis of a specific strikeline, toward analysing it using prior physical knowledge. A

novel implementation of a network from the U-Net family is introduced for the first time in this paper. This network is specifically designed for the joint estimation of two scalar features to the strikeline, and a 2D map of hot point locations from a single ROI image containing a strikeline. The modified UNet, which is trained to minimize a specific loss value, is utilized to predict the shape of strikelines through curvature and angle, as well as the location of all contained hottest points, regardless of their quantity.

Outline

This paper is structured as follows: Sect. [Overview of the WEST Tokamak and Hot Spot Issues](#) introduces the WEST tokamak and discusses the challenge of wall protection. The various objectives and contributions of this study are detailed in Sect. [Objectives and Contributions](#). The creation of the synthetic dataset is the focus of Sect. [Dataset Generation](#). Section [Implemented Structure](#) outlines the structure that has been developed and implemented to tackle the identified issues. Lastly, Sect. [Evaluation](#) list the results and explores the potential application of the method to real-time analysis.

Notations

Throughout this paper, the following notations are used: \mathbb{P} is a probability distribution, while μ and σ correspond respectively to the mean and standard deviation of the distribution. Y denotes an image label (and \hat{Y} the associated predictions) and y a scalar label (and \hat{y} the associated prediction).

In the context of this study, a terminological convention is adopted when discussing the Tversky loss. The term "Tversky loss" is used, but it actually refers to its complement, $1 - \mathcal{T}$. This modification allows for the interpretation of the value as decreasing with enhanced performance of the model in the segmentation task.

All the IR images use the "coolwarm" linear colormap. The interval given for the colormap extends from the temperature of the darkest point to that of the brightest point.

Notation $[a:b]$ stands for an interval of real values between scalars a and b ; $\{a,b,c\}$ denotes a discrete set of three scalar values a , b , c .

Overview of the WEST Tokamak and Hot Spot Issues

WEST Tokamak

WEST, or Tungsten (chemical symbol "W") Environment in Steady-state Tokamak, is a French tokamak that began originally operating as Tore Supra in Cadarache, South of France.

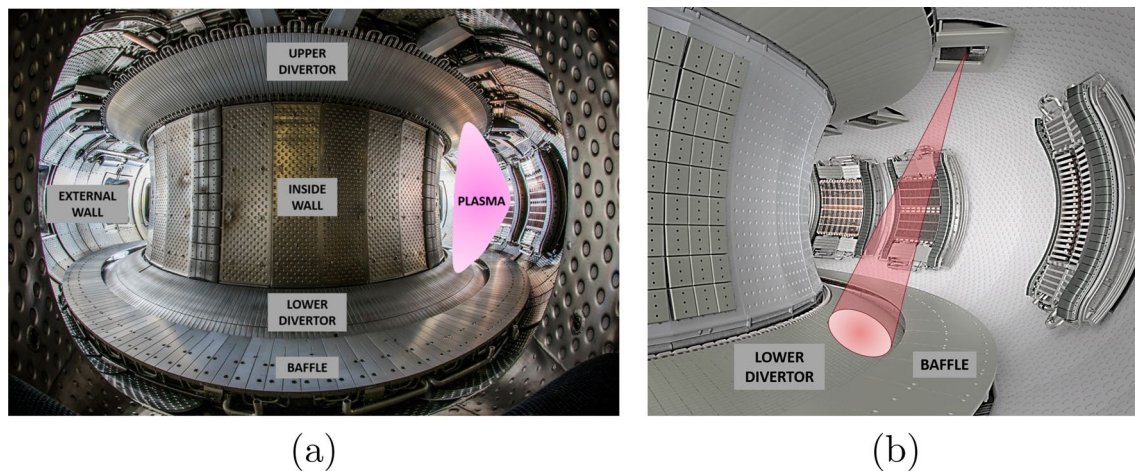


Fig. 1 Photo of the interior of the WEST Tokamak including the description of areas (a). Simplified 3D reproduction of the tokamak with a divertor sight-of-view IR camera (b)

This device underwent a major upgrade to install tungsten walls and a divertor, and the machine was transformed from a French national experiment to a European user facility in the decade 2010. Tore Supra was renamed WEST to better affirm the change of machine and status. WEST validates and fatigue-tests the ITER actively cooled tungsten divertor components (called Plasma Facing Units PFUs) during the ITER construction phase and prepares their safe operation.

Plasma Facing Components Monitoring

Monitoring the tokamak internal wall and divertor is crucial to obtain long-duration plasma. These hot spots can take various forms, including “strikelines”, “electron type 1”, “ripples loss” or “Unidentified Flying Objects” (UFOs), which may result from the pulverization of wall armour and subsequent detachment of metal dust. A local WEST-related reduced taxonomy is currently in use at WEST and has proven effective for development activities (a full taxonomy of hot spots is still being developed in the framework of a cross-machine activity).

Optical measuring instruments are used to oversee the internal wall and divertor, which play the role of thermal shields. They provide the armour surface temperatures during operation. They are made of fixed optical endoscopes, which provide a field of view of a section of the machine internal wall. The detector is an Infrared camera. These systems allow for the observation of approximately 50% of the entire internal wall, while the remaining portion is monitored either passively or indirectly. Specific viewing systems are present at WEST, including a high-resolution view of the divertor with 0.1 mm spatial resolution; and two complementary views of the divertor (direct view through a

window, scheme on Fig. 1). This Infrared viewing diagnostic is described by Courtois et al. in [14].

The “Strikelines” are the most prevalent hot spots. They result from the normal power deposition on the divertor (top or bottom). The strikelines are located at the contact zone between the divertor and the plasma.

Figure 2 illustrates an infrared image of the lower divertor during a pulse. The lower half of the image is an extension of its upper region: due to the divertor’s large aspect ratio along the entire length of the tokamak, capturing a 60° sector within a single field of view results in inefficient usage of the detector. Two separated lines of sight and a recombination prism are employed to better fit the FoV of a 60° divertor sector within the detector.

As shown in Fig. 2, these strikelines are discontinuous and exhibit a cosinusoidal modulation, with the peak value

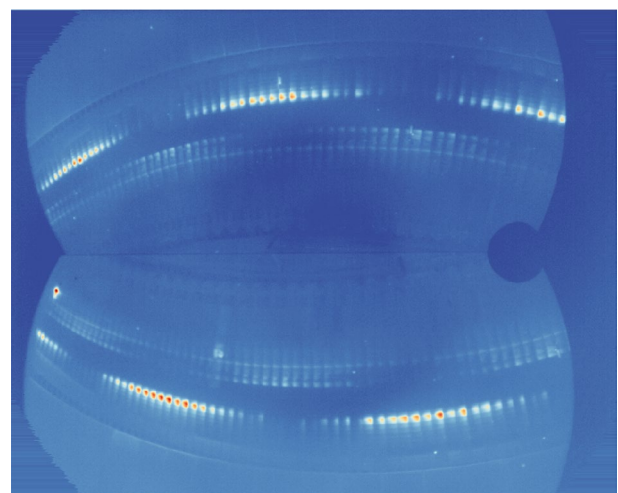


Fig. 2 Divertor camera (DIVQ2B) for pulse 57396. ‘Coolwarm’ colormap [100;300 °C]

situated at the strikeline's centre. This is caused by the discrete arrangement of the 18 toroidal magnetic coils on the WEST tokamak which results in a toroidal modulation of the toroidal magnetic field (the so-called "ripple effect"). Strikelines display a characteristic "croissant" shape, with a series of local hotter spots resulting from the series arrangement of plasma facing units.

Abnormal divertor temperatures arise from several potential causes: the most frequent causes are a deteriorating thermal contact to the cooling circuit, growth of a resistive thermal deposit at the surface of the armour tile, or possible tile or PFU misalignment, either pre-existing or occurring following deterioration of the fixture of the PFU.

Additional temperature anomalies do occur due to erosion or dust deposition on the divertor, or other causes. When tungsten blocks are damaged to an extent that their outer layers are altered, the emissivity of the armour material changes, thereby altering the apparent temperature obtained by the IR camera. Similarly, dust deposits on a machine in the field of view can accumulate on the divertor at ground level and modify the emissivity of certain zones, resulting in abnormal strikelines (see Fig. 10). These phenomena can be observed when studying the divertor after an experimental campaign.

Existing Pipeline for Thermal Events Analysis on WEST

A measurement and acquisition chain is in place. It encompasses the conversion from raw digital levels to temperature, acquisition, storage, and data access [15]. The expert analysis of hot spots by human operators considers numerous parameters and factors, such as their shape, extent, potential structure, temperature value, and temporal correspondence with other machine events. Besides data accessible by direct or indirect measurements, the analysis of hot spots relies on prior knowledge of past thermal events and synthetic images produced from first principle physical models (digital twins).

Automated infrared data processing has been a focus at the IRFM Infrared laboratory for over a decade, complementing human expertise. Real-time monitoring is used based on images from infrared cameras in the Wall Monitoring System (WMS). Feedback control uses temperature thresholds defined upon Regions of Interest (ROI) according to components allowable. Control laws are implemented to monitor and feed back on actuators if control thresholds are exceeded. These basic controls are currently in use but are rudimentary and subject to false positives [8].

Investigations into more advanced controls using artificial intelligence and deep learning are underway. An end-to-end pipeline is being developed to detect and classify hot spots

[13, 16] based on recognisable features like hot spot shape, position, and temperature distribution, possibly combined.

The novel model introduced in this article is integrated into this hot spot processing pipeline. The existing pipeline provides bounding boxes around the detected hot spots, along with a class associated with each hot spot. These bounding boxes are used as input, for an objective that is described in the Sect. [Objectives and Contributions](#).

Objectives and Contributions

The research team is currently focused on the development of a pipeline for the detection and classification of hot spots, which has proven to be both functional and efficient. The aim of this work is to extract new information from infrared images, with an emphasis on acquiring knowledge that closely mirrors the insights of a human expert. This approach is particularly relevant in the field of wall protection and non-destructive control, where experience from previous operations plays a crucial role. Therefore, incorporating such prior knowledge into the development of new models is considered beneficial. This general objective is applied, in this article, to the extraction of novel information pertaining to strikelines, which are significant hot spots in the WEST tokamak and, more broadly, in fusion reactors equipped with a divertor.

Strikeline hotspots present a rich source of information. The data chosen for analysis closely mirrors what a human infrared expert would extract when examining a strikeline. The infrared expert, tasked with inner wall protection between each discharge during the experimental campaigns, often automatically and subconsciously analyses the structure and temperature distribution within the strikeline. Experts were willing to have access automatically to novel physical data from the strikelines, using the pipeline's detections as inputs.

The strikelines are a good hot spot class for investigating possible technique toward injecting a priori knowledge in detection/classification, because they are numerous and the a priori knowledge is widely shared, and can be formalised into numbers. In addition to the data already produced by the existing pipeline, in the form of bounding boxes, the research axe was selected to extract two novel physical features from the strikeline, using the pipeline's detections as inputs. These are the curvature of the strikeline and its angle relative to the horizontal. The term "curvature" in the context of the strikeline is associated with its visual manifestation on infrared camera. This is due to the diagnostic setup, which results in the strikelines exhibiting a curvature that imparts a "croissant" shape following the divertor disposition. While it is challenging to accurately compute a curvature index on the hot zones of this shape, it

remains feasible to assign a “score”. This could potentially facilitate the classification of strikeline curvatures into, for instance, four distinct categories. The strikeline’s angle is another characteristic associated with the image derived from the infrared diagnosis. This measures the angle between the horizontal and the tangent to the strikeline. It is understood that a typical strikeline, observed on WEST tokamak IR diagnostics, possesses a non-zero curvature and an angle that can vary from 0 to approximately thirty degrees. For example, a human expert would immediately label a strikeline with extreme curvature as being abnormal (that means, further human expertise would be required to better understand the cause of such extreme curvature. Or discard the strikeline as being a rare artefact, not worth further investigation).

The method presented in this article aims to answer a multi-task learning problem. On the one hand, it encompasses a regression part aimed at obtaining the actual physical values of the curvature and angle. On the other hand, a segmentation component is involved, which seeks to identify the hottest zone (one pixel) of each PFU for the purpose of counting them and analysing the temperature.

Neural networks are an effective approach to multi-task problems. Certain network designs can indeed learn both regression and segmentation elements. In contrast, a standard method of image processing necessitates running two separate pipelines to perform the required calculations independently. Given the nature of the problem, the segmentation task could potentially be the most challenging. As a result, it is selected to design a network that has demonstrated its effectiveness for segmentation, and then enhance it to also yield the desired regression outcome.

U-Net, a type of convolutional neural network, was originally developed for biomedical image segmentation in 2015 in [17]. It is an architecture with a contracting path and an expansive path, with the aim of performing semantic segmentation. Today, U-Net and its variants are widely used in various fields. In medical image segmentation, U-Net is the most widespread image segmentation architecture due to its flexibility, optimized modular design, and success in all medical image modalities. It has been used in CT scans, MRI, X-rays, and microscopy... Thus, U-Net has proven to be a versatile tool in the field of deep learning, with its use extending beyond its original purpose of biomedical image segmentation [18]. As highlighted in [19], U-Net are mainly used for segmentation tasks. However, this network structure possesses the potential to execute a multitude of other tasks such as classification or regression.

Section **Implemented Structure** proposes a novel architecture, referred to as “Constrained U-Net”. This architecture is designed to deliver multiple types of outputs: a segmented mask and scalars, using a strikeline thumbnail as input. The method introduced in this article serves

multiple purposes. It aims to address the challenge of multi-output types while maintaining a network that incorporates physical knowledge and offers an inference speed suitable for potential real-time requirements.

To date, no literature has been identified that addresses both segmentation issues and ‘global’ regression at the image scale (i.e. predict a vector of scalars from the entire image in output) within a single network. While UNETs have been employed for pixel-scale regression [20] and image-scale regression [21], these applications do not incorporate any segmentation tasks.

Dataset Generation

The decision to associate this work with the generation of simulated data was made for multiple reasons. Firstly, defining a universal method for calculating the angle and curvature of each strikeline presents a significant challenge. Additionally, the process of labelling the hottest pixels is extremely time-consuming, as it necessitates the identification of approximately fifteen pixels (to the nearest pixel) per image. Considering the substantial number of images required for annotation in training, the creation of a dataset of pixels annotated by a human expert is impractical as each experimental campaign generates terabytes of uncompressed infrared video data.

An additional significant factor that influenced this decision was the limited diversity in the real-world images. Given that the majority of real strikeline images have a strong resemblance to each other, estimating a network’s ability to generalise based on low diversity becomes quite complex. The generation of a synthetic dataset introduces more variability in the physical parameters, even if it results in the creation of ‘improbable’ hotspots. The objective of this dataset generation, nonetheless, is to maintain the strikeline structures in close resemblance to the actual images such that it is conceivable that training on simulated data and application on real-world images could be possible.

Generation of the Strikelines

The neural network structure proposed in Sect. 5 requires a fixed input image size. This dimension is determined by computing the median of the lengths and widths of over 45,000 boxes identified by the existing pipeline. Consequently, generated images produced by the method described here have a dimension of 120x50 pixels. This ensures an equal number of “zoomed” and “de-zoomed” images when the method is integrated into the existing pipeline. This balance is key to prevent any learning bias that could potentially degrade performance on real-world images. The generation

process adheres to some of the principles delineated in [22], but it exhibits greater sophistication in terms of the diversity of images produced.

Stage of the Creation Process

The process involves several steps:

1. A 1D profile of heat flux and temperature distribution on the surface of a PFU monoblock is generated using CAST3M [23] thermal calculation code from physical input parameters from the WEST tokamak.
2. Monoblocks and their temperature distribution are multiplied horizontally to generate a 1D line with N monoblocks. The physical gap present on the WEST divertor is added between each monoblock by artificially inserting points at 70°C (machine base temperature). This horizontal direction serves later as “toroidal” direction.
3. The 1D line is developed vertically to create a 2D image of N PFUs with identical distribution along the entire vertical and repeated patterns between all monoblocks. The vertical axis serves later as poloidal direction.
4. In the toroidal direction, a cosine filter is employed to simulate the Ripple effect (see Sect. [Plasma Facing Components Monitoring](#)).
5. Eich flux distribution laws [24] are applied on toroidal and poloidal axes respectively to impose toroidal field ripple modulation around tokamak and flux intensity at plasma-PFU contact. In order to closely mimic the infrared images obtained during the tokamak campaigns, it might be useful to avoid applying the Eich filter to the same vertical point of each PFU. This approach would result in entirely ‘straight’ strikelines, which do not accurately represent the circular nature of the divertor. Therefore, during this phase, it is feasible to introduce what is termed as the “curvature” of strikelines. To establish this curvature, the lowest point of application on the left of the image and the highest point of application situated at the centre of the strikeline are required. A circle is then drawn through these two points to identify the location where the Eich filter will be applied vertically. Four states of curvature are then defined, ranging from state 0, where the stripe is straight, to state 3, where the stripe exhibits abnormal curvature. In appendix A, an example of different curvatures of a same base strikeline is provided.
6. A pixel/cm filter matching the resolution of IR cameras defined in [14] is applied.
7. At this point, a synthetic image of the desired size, 120x50px, is generated. To increase the diversity of the images and to match as closely as possible the images

obtained during campaigns, it could be beneficial to rotate the image. Indeed, infrared cameras have a fairly wide angle of view. For example, the strikeline visible on the left of the image is not angled in the same way as the one right in the centre of the image. This discrepancy is attributed to distortion, as the pixels visible in the final image are have a variable distance to the optics pupils. Consequently, the image undergoes a rotation ranging from 0 to 90 degrees. The interval is reduced between 0 and 90 because for the other zones of the divertor sight, a simple axial or central symmetry permits reference to an angle of 90°. This rotation is implemented using a rotation matrix and linear interpolation.

The entire process results in a total of 32,400 strikeline images divided randomly into 3 sets (train, validation and test with respectively 22680, 6480 and 3240 images). Each image is 120x50 pixels.

Physical Parameter Variations

This technique of strikeline generation allows for direct integration of varying degrees of a priori physical/structural knowledge, namely strikeline curvature, angle, number of PFUs and temperature. Other calculation codes are available for the purpose of obtaining thermal patterns (PFC Flux [25], Smither), offering both greater physics accuracy in generating strikelines and being more recognised in the science community, but they lack the ability to conveniently include or exclude certain physical parameters (curvature, angle) being needed for this work.

The selection of these parameters is designed to strike a balance between producing strikelines that closely resemble real images and maintaining physical relevance. Consequently, four physical parameters have been chosen, which are varied across broad value intervals to generate a diverse set of strikelines (see Table 1).

Adding Noise

The image ‘background’ of experimental tends to be somewhat noisy at the lower end of the measurement range. Noise is introduced into the simulated images, to better replicate these images and to avoid learning of overly ‘perfect’ images.

Noise addition is done using an additive Gaussian white noise. It has a normal distribution $\mathcal{N}(0; 0.05 \sigma_{training_set})$, where $\sigma_{training_set}$ represents the standard deviation of all the pixels of the training dataset. An example of the application of this noise is provided in Fig. 3.

Table 1 Range of values of physical features for strikelines generation

Physical feature	Range of values
Max temperature	[400:2000] °C
Number of PFUs	{6,8,10,12,14}
Curvature	{0,1,2,3}
Angle	[0:90]°

Pre-processing

According to the methodology exposed in [13], uniformity shall be maintained in the normalization process applied to the images. This is in accordance with the project's nested structure. Consequently, the following approach is adopted for normalizing the entire dataset:

$$px_{norm} = \frac{px - \mu_{training\ set}}{\sigma_{training\ set}} \quad (1)$$

With px , the pixel to normalize and $\mu_{training}$ & $\sigma_{training}$ respectively the mean and standard deviation of all the pixels of the training dataset.

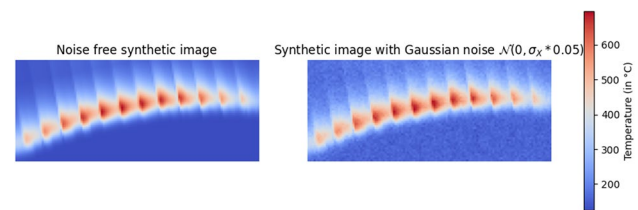
For the regression labels, normalization between 0 and 1 is implemented to enhance the stability and convergence speed of the network.

Implemented Structure

Constrained U-Net

This novel architecture, termed as ‘‘Constrained U-Net’’, has been designed to tackle the dual challenge of segmentation and regression within a single network. This network is structured in the form of a traditional U-Net, comprising a descending segment, a bottleneck, and an ascending segment with skip connections. Regarding the U-Net's structure, four downsampling stages are implemented to maintain the network's efficiency. This level of downsampling is deemed adequate for the segmentation, considering the relatively minor variations present in the infrared images obtained from the tokamak. ReLU activation function is used in the network's layers. In the output section related to the mask, a sigmoid function is implemented, which provides a value for each pixel within the range of 0 to 1, thereby aiding in the segmentation process (Fig. 4).

The innovative aspect of this architecture lies in the constraint applied to the information within the bottleneck. The extraction of the physical parameters is executed through a conventional ‘‘dense’’ neural network. This dense network takes as its input the extraction of the input image (1024

**Fig. 3** Example of noise addition on a synthetic image

values), and outputs two floating values, which represent the targeted physical features. The benefit of this network architecture lies in the interchangeability of the physical features extracted from the bottleneck. By retraining the network with appropriate labels corresponding to a new feature, it becomes feasible to change the output type of the dense network. This extracted features are used for regression analysis, thereby providing physical insights into the image structure, such as the angle and curvature of the hot spot.

The output of the network comprises three components: an image shaped mask that indicates the location of the most intense pixels within each hot sub-region, the value of the angle in degrees, and a curvature index.

The feature extraction at the bottleneck level, coupled with the integration of regression into the overall loss function (discussed in Sect. Loss Function), enables the U-Net to be ‘‘constrained’’ to preserve information that holds physical significance during its downsampling process.

Loss Function

In this study, a composite loss function \mathcal{L} (Eq. 2) is employed to optimize the model. This loss function is a weighted sum of Tversky loss (Eq. 3) and Mean Squared Error (MSE) loss (Eq. 4). The Tversky loss is a generalization of the Dice coefficient and Jaccard index, and is particularly useful for handling imbalanced datasets [26].¹ The Tversky loss function addresses image-level imbalance, a common issue where the count of positive pixels significantly outweighs that of negative pixels (or vice versa) in a image. In this work, the Tversky loss function is employed in a batch-wise configuration. The batch-wise method tackles batch-level imbalance, a situation where only a few pixels in the batch are positive. By taking the loss over the entire batch, it ensures that even if there are only a few positive pixels in the whole batch, an all-zero prediction - which can easily become a local minimum in the case of imbalanced data - will be significantly distanced from the optimum. Moreover, the utility of this function in the given context is underscored by the flexibility it offers

¹ For a full explication of Tversky loss, see [27]

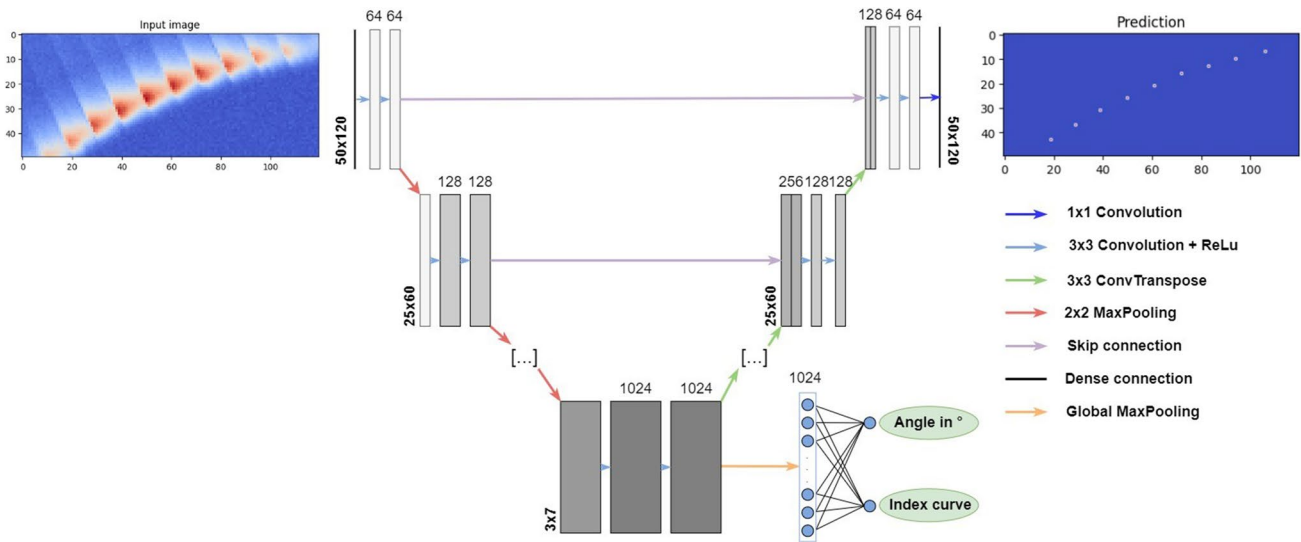


Fig. 4 Constrained U-Net architecture

in adjusting the 'α' and 'β' coefficients. These adjustments can effectively influence the 'importance' attributed to false positives and false negatives. Section 6.2 will elaborate more on the machine operation benefits that can be achieved through these coefficient modifications. This Tversky loss is a part of the global loss \mathcal{L} and is multiplied by a coefficient 'τ' to control its contribution to \mathcal{L} .

On the other hand, the MSE losses measures the average squared differences between estimates and actual values, providing a measure of regression performance. It is scaled by a factor 'ε'. By combining these two losses, the loss function can effectively balance the trade-off between image segmentation performance (via Tversky loss) and regression accuracy (via MSE loss).

$$\mathcal{L} = \tau(1 - \mathcal{T}_{\alpha,\beta}(Y_1, \hat{Y}_1)) + \epsilon(MSE(y_2, \hat{y}_2) + MSE(y_3, \hat{y}_3)) \quad (2)$$

$$\text{with } \mathcal{T}_{\alpha,\beta}(Y_1, \hat{Y}_1) = \frac{Y_1 \hat{Y}_1 + \delta}{Y_1 \hat{Y}_1 + \alpha(1 - Y_1) \hat{Y}_1 + \beta Y_1 (1 - \hat{Y}_1) + \delta} \quad (3)$$

$$\text{and } MSE(y, \hat{y}) = (y - \hat{y})^2 \quad (4)$$

where $\hat{Y}_1 \in [0:1]^{6000}$ corresponds to the segmented output image of the U-Net. This image of size 120×50 is composed of 6000 values between 0 and 1. The closer the value is to 1, the more the network is "confident" that the pixel is the hottest pixel in the PFU.

$\hat{y}_2 \in [0:3]$ is a scalar corresponding to the prediction of the curvature.

$\hat{y}_3 \in [0:90]$ is a scalar corresponding to the prediction of the angle of inclination of the strikeline. This angle is in $^\circ$.

In the training process of the network, both loss functions are incorporated during back-propagation. The objective is to ensure that the initial convolutional layers do accentuate the main features for segmentation while also facilitating the prediction of specific physical values. The U-Net is consequently "constrained" to preserve physical/structural information in the initial convolution layers to facilitate a decrease in the regression loss which influences the gradient descent of the overall loss function.

Investigation into the Determination of Optimal Network Dimensions

This section addresses the determination of the best network dimensions. Constant values are maintained in this investigation for all parameters that influence learning, such as the learning rate, epochs, batch size, loss function coefficient, and others. The only variable being changed is the sizes of the 2D convolution layers, specifically the number of filters. This approach results in networks of varying sizes, each with a different number of parameters to learn. Larger networks have the potential for increased efficiency but may also experience a significant increase in inference time. Therefore, the objective is to find an optimal balance between performance and speed. The results are summarised in Table 2.

A suitable network structure is selected based on the evaluation of the loss functions for various models. The most extensive network (1) demonstrates proficiency in learning the regression component, yet it fails to generalize effectively for mask segmentation. This limitation is attributed

Table 2 Results comparison on validation dataset of 5 networks with different number of trainable parameters

Networks	5	4	3	2	1
Number of trainable parameters	33,997	540,331	2,158,931	34,514,243	138,037,891
Epochs	250	250	250	250	250
α	1	1	1	1	1
β	0.9	0.9	0.9	0.9	0.9
τ	1	1	1	1	1
ϵ	0.5	0.5	0.5	0.5	0.5
$1 - \mathcal{T}_{\alpha,\beta}$	$5.3 \cdot 10^{-1}$	$2.7 \cdot 10^{-1}$	$2.2 \cdot 10^{-1}$	$6.5 \cdot 10^{-2}$	$9.9 \cdot 10^{-1}$
$MSE(y_2, \hat{y}_2) + MSE(y_3, \hat{y}_3)$	$1.0 \cdot 10^{-2}$	$3.0 \cdot 10^{-3}$	$2.0 \cdot 10^{-3}$	$4.0 \cdot 10^{-4}$	$6.0 \cdot 10^{-5}$
Av. time to process 1 image (s)	$4.4 \cdot 10^{-3}$	$4.5 \cdot 10^{-3}$	$5.2 \cdot 10^{-3}$	$5.3 \cdot 10^{-3}$	$8.5 \cdot 10^{-3}$
Inference capacity (fps)	226	219	190	188	116

to insufficient learning time. Network 5 is also unsuitable, as evidenced by its relatively high segmentation and regression values. The size of this network may be too small to extract all the necessary features for effective segmentation and prediction of physical quantities.

Networks 3 and 4 exhibit similar results, which are relatively good, yet they are significantly outperformed by Network 2. Despite the substantial size difference between Networks 2 and 3, their inference times are quite comparable. Therefore, for this project, Network 2, with its 34 M parameters, emerges as the preferred choice due to its superior performance and sufficiently rapid inference time for the requirements (see Sect. 6.4).

Evaluation

Network 2 has been selected for the evaluation of the proposed constrained U-Net. Subsequently, two versions of Network 2, termed as Networks A and B, will be compared. These networks correspond to two versions of the Tversky loss. Additionally, a comparison will be made between Networks A and B, the "Classical U-Net", and a max-tree [28] based segmentation method.

Comparative Methods

Two comparative analogous methods are employed for the purpose of evaluating the model presented in this article. These methods, provide a basis for comparative analysis and bear similarities to the model. The two methods are "segmentation only" techniques. The comparative analysis is conducted based on the segmentation outcomes derived from the hot spot images of the test dataset. They are the following:

- **"Classical U-Net"** The U-NET architecture has been specifically developed for the purpose of image segmentation. So comparing the segmentation results of

the Constrained U-NET with a 'classic' U-NET makes sense. The question arises whether this addition on the Constrained U-Net impacts segmentation positively or negatively. In an effort to assess the influence of the regression module, the overall U-NET architecture was retained as a benchmark. The only change implemented was the exclusion of the dense network tied to regression, along with the corresponding term in the loss function. This strategy facilitated a concentrated examination of the regression module's impact. New physical features are deducted from the image, but it is important to ascertain whether this is correlated with a reduction in segmentation performance.

- **Max-tree for segmentation** Max-tree is used as a comparative method that does not rely on neural networks. The max-tree method is a technique frequently employed in medical image segmentation. It is proposed by Dr. Salembier in [28] towards the end of the 90 s. The basic concept aligns with the one described in [22], where the apex of each "branch" surpassing a certain threshold is identified. Rather than analysing these branches globally to infer a potential anomaly, here, only the hottest pixel of each branch is recovered, which will become the segmentation prediction for this method. The primary drawback of this method is its reliance on the branch splitting threshold value. Indeed, if the threshold is set too high, there is a risk of overlooking hot zones situated at the extremities of the strikeline, as these areas are considerably cooler than the central zones. On the other hand, if the threshold is set too low, an excessive number of branches may be selected, potentially leading to a high incidence of false positives. A direct correlation is observed between the threshold of branch cutting and the quantity of points segmented via the employed methodology. A comprehensive study could be conducted to devise a method for implementing an adaptive threshold. The reasoning could also be based on a fixed number of cut branches. This approach, however,

would consistently yield the same number of segmented points, which could be seen as a disadvantage. In fact, a priori knowledge of the number of PFUs that will be activated by the plasma on the divertor is not available. This advantages neural network methods, which do not necessitate a threshold. Therefore, the same threshold as the one used in [22] (Sect. III.D) is adopted here.

Results on Test Dataset

In the results section, two similar Constrained U-Net are examined. These networks share identical characteristics. They have been selected based on specific hyper-parameter tests. The distinction between the two lies in the coefficients used in the Tversky loss function. Network A uses an α value of 1 and a β value of 0.9, indicating a slightly higher emphasis on false positives. Conversely, network B operates with an α value of 0.9 and a β value of 1, thereby placing a slightly greater emphasis on false negatives. The objective is to evaluate the effect of these minor coefficient adjustments on the recall and precision outcomes derived from the test dataset. While it is feasible to extend this study by drastically unbalancing the two coefficients, the relevance for hotspot monitoring is limited. However, providing an option for a slight 'direction' for the network is logical. From a security perspective, false negatives pose a risk as they indicate missed PFUs, which could potentially become anomalously hot. Conversely, in the context of physics research, false positives can be problematic as they may skew studies of a PFU's cooling time, for instance. The Tversky loss function facilitates a degree of modularity in the segmentation component of the U-Net, proving beneficial in a field where security and physical studies intersect.

The characteristics of the chosen network, which will be used for all results in the following sections, are outlined in the Table 3:

From a quantitative perspective, the results of the two loss functions associated with regression and segmentation are presented. For the segmentation, the Accuracy metric may not be particularly meaningful due to the class imbalance. Indeed, a network that does not predict any hotspots

on an image with 8 PFUs would have an accuracy of 99.8%, which could appear very good from an external perspective, even though the network predicts an image without PFUs. To obtain more meaningful metrics, it is necessary to use Precision, Recall, and the F1-score. For regression, the Mean Absolute Error (MAE) for the two physical quantities can be added to provide a more physically meaningful interpretation. These are summarized in Table 4

The model's performance on the simulated data is highly satisfactory. Metrics such as precision, recall, and F1 score hover around the 99% mark, a critical factor in the context of operational safety. As for regression, the predicted values exhibit remarkable accuracy, with an average error of less than 1° for the angle and less than 0.05 for the curvature index. A more graphical representation (see Fig. 5) of the different predictions for both physical features on the test set can be provided. This is achieved by plotting the prediction as a function of the actual value, which allows for a visualisation of the distribution and spread of the predicted values.

The predictions of the physical features exhibit no outliers. This is a significant and positive observation, confirmed by the computation of Pearson coefficient R^2 for both distributions: $R_{(a)}^2 = 0.998$ and $R_{(b)}^2 = 0.995$. Having no outliers is particularly crucial for a method designed to inform machine safety decisions, where outliers could potentially result in erroneous conclusions. The distribution of error in angle estimations is relatively uniform, although there is a minor tendency to underestimate the actual angle between 60 and 80 degrees.

Regarding curvature, it is noteworthy that there are no data points around 0.5, 1.5, and 2.5. These regions do not permit a swift determination of the strikeline's curvature. Despite this, it is beneficial to retain the predictions as floating-point numbers. The values at .5 could potentially signify an intermediate point detected by the network, thus providing valuable insights.

Comparative analyses for the segmentation task favour the constrained U-Net over the comparative methods. This outcome could be expected as the max-tree method would necessitate adaptive thresholding (which could be challenging to achieve), to maintain a consistent number of predicted pixels. The U-Net method without regression yields results that are closely aligned with models A and B, albeit slightly inferior. This gap could potentially be bridged with additional hyper-parameter tuning on the non-regression network. As discussed in subsection 6.1, this U-Net has not been reconfigured to be optimized for segmentation. The key takeaway from this study is that the regression component does not significantly impede segmentation, while concurrently enriching the model with new information from the regression.

Table 3 Networks hyperparameters

	Network A	Network B
Number of parameters	34514243	34514243
Number of epochs	1000	1000
Learning rate	0.001	0.001
Batch size	256	256
α	1	0.9
β	0.9	1
τ	1	1
ϵ	0.5	0.5

Table 4 Network results on Test dataset

Metric	Network A	Network B	Classical U-Net	Max-tree
$1 - \mathcal{T}_{\alpha,\beta} (\alpha, \beta = 1)$	0.025	0.034	0.241	0.755
$MSE(y_2, \hat{y}_2) + MSE(y_3, \hat{y}_3)$	1.006	0.699	–	–
Precision (threshold 0.5)	0.993	0.985	0.883	0.396
Recall (threshold 0.5)	0.982	0.980	0.851	0.392
F1-Score (threshold 0.5)	0.987	0.983	0.863	0.394
MAE Angle (in°)	0.787	0.667	–	–
MAE Curvature	0.050	0.023	–	–

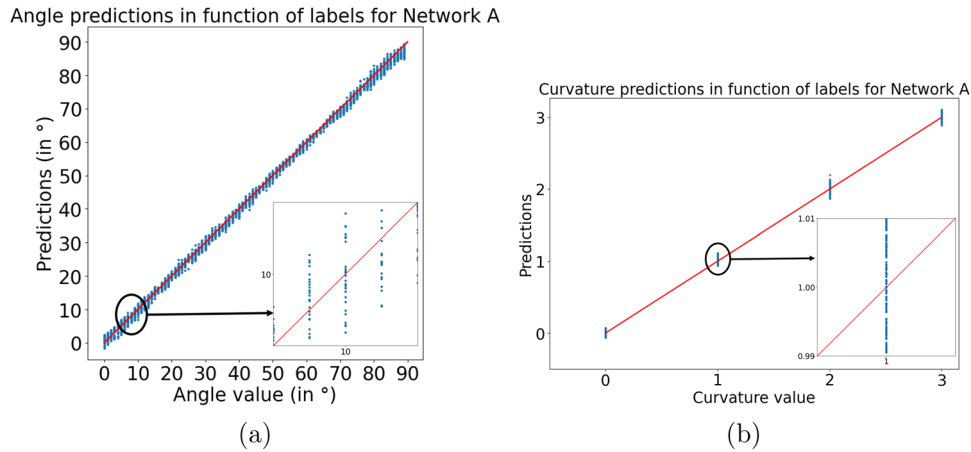


Fig. 5 Distribution of angle (a) and curvature (b) predictions as a function of the true value

From a qualitative perspective, Appendix C presents the outcomes of all these models on a test set image. This image closely resembles the potential output from the hot-spot detection pipeline, with the curvature, angle, and number of PFUs falling within the 'normal' value ranges.

Both Models A and B exhibit remarkable accuracy, inclusive of their ability to predict the values of curvature and angle. Model A holds a slight edge as Model B fails to detect the 4th PFU from the left. For the comparative methods, the conventional UNET demonstrates satisfactorily performance, albeit with two potentially dangerous false negatives. Interestingly, no false positives are predicted, which could be beneficial for potential supplementary physics studies. Max-tree based method is interesting, but the noisy nature of the images results in several sub-branches originating from the same hot zone. Consequently, it is not feasible to obtain a single pixel predicted by PFU with a single threshold at the image scale. This leads to the presence of potentially serious false positives, as well as false negatives on lower temperature values.

Qualitatively, it could prove insightful to present some results derived from the model A's performance on the test set:

The two results shown here (Figs. 6 and 7) are extracted from the test dataset and are highly accurate. The predicted

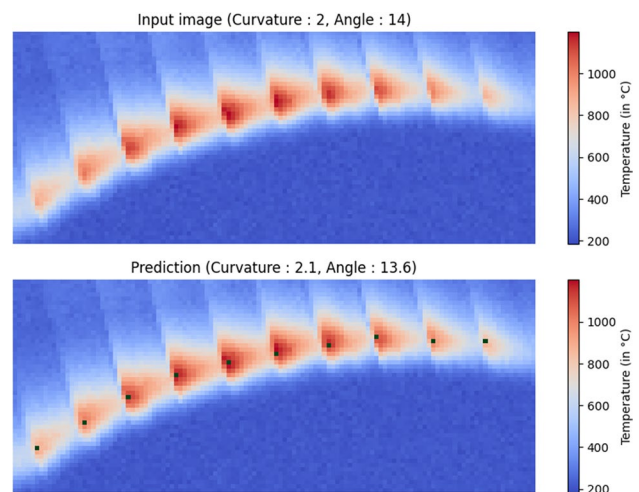


Fig. 6 Top - Input image visualized with coolwarm colormap; Bottom - segmentation result with dark pixels indicating segmented regions. Titles contain regression labels (top) and predictions (bottom)

physical values for both images are extremely close, if not identical, to the values used to generate the image. Regarding image segmentation, the first image is flawless with all detected

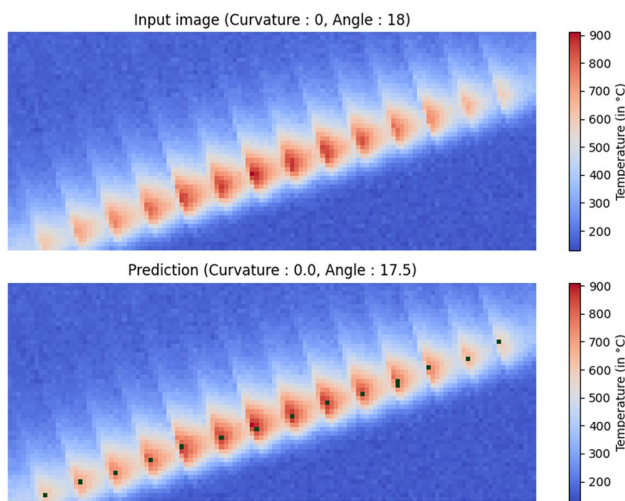


Fig. 7 Top - Input image visualized with coolwarm colormap; Bottom - segmentation result with dark pixels indicating segmented regions. Titles contain regression labels (top) and predictions (bottom)

pixels being accurate. However, in the image of Fig. 7, a discrepancy is observed in the fourth PFU (from the right) where the network predicts two pixels on the same PFU. In this example, the two predicted pixels have similar temperatures (745 and 747 °C), it can be hypothesized that this could lead to the network's inability to make a distinct "choice".

These qualitative and quantitative results on the test dataset provide a level of confidence in the network's performance across various types of simulated images. This substantiates the concept of employing a physics-constrained multi output method to address the challenge at hand.

An key question that arises is whether this same network would be capable of predicting the desired outputs on real images. This supposition entails two significant considerations: the simulated image dataset must closely resemble real images, and the network should not have over fitted the simulated images, thereby retaining its ability to generalize to images that exhibit slight differences in structure and temperature distribution.

Usage of the Constrained U-Net on WEST Tokamak Real Images

The constrained U-net is applied to real images. Real images undergo the same transformations, including normalization and resizing, before being fed in the network A. The generated prediction are given in Figs. 8, 9 and 10.

Beginning with an analysis of Figs. 8 and 9, it is observed that the predicted regression values are consistent. The two strikelines originate from different areas of the sight. The strikeline in Fig. 8 is derived from the centre of the sight, resulting in a less angulated and less curved strikeline due

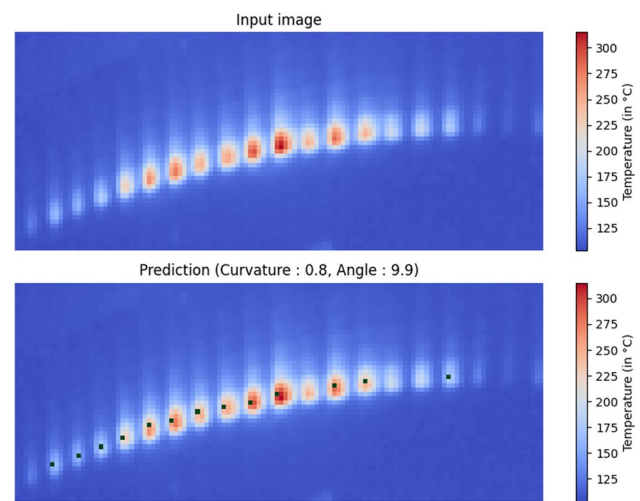


Fig. 8 Example on a real strikeline extracted from C7 campaign in January 2023 (57396 - DIVQ1B)

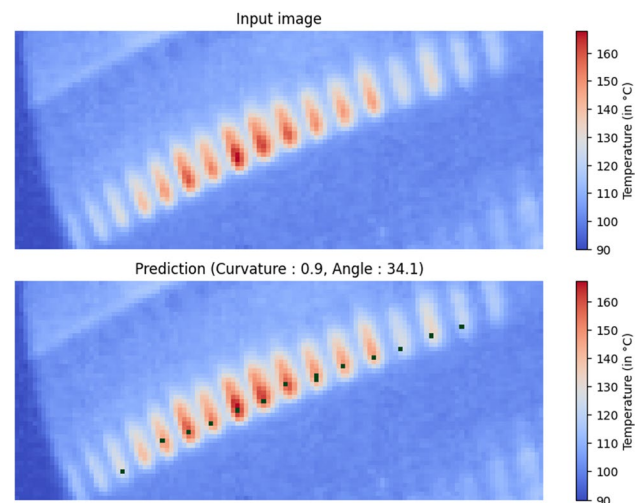


Fig. 9 Example on a real strikeline extracted from C7 campaign in January 2023 (57438 - DIVQ2B)

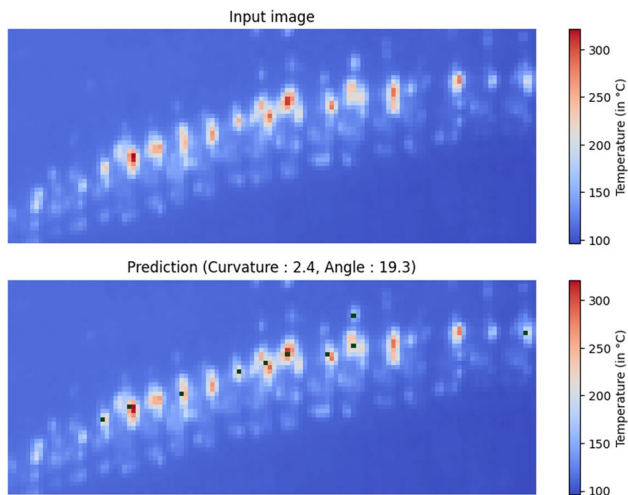
to the angle of sight. Conversely, the strikeline in Fig. 9 is extracted from the upper left part of a divertor sight, leading to a more angular and curved strikeline.

Precise values for the curvature and angle of the strikelines are not available on real images. However, by applying the same principles used for the curvature of synthetic images, the curvature of these two strikelines can be estimated to be slightly below the value 1. The angles can be estimated using trigonometric principles directly applied to the image. Specifically, the angle of strikeline 8 is estimated to be 9°, while the one of strikeline 9 is estimated to be 28°.

In the regression analysis, manual labelling can be accomplished by retrieving the values for each pixel and

Table 5 Quantitative results on 2 real-world images

	Fig. 8	Fig. 9
True positives (TP)	4	7
False negatives (FN)	12	8
False positives (FP)	9	7
Pairs of FP/FN located at less than 1px apart	9	6

**Fig. 10** Example on a real strikeline extracted from C7 campaign in April 2023 (58502 - DIVQ1B)

marking the hottest pixel in each PFU. This process is notably time-consuming, prompting the exploration of an alternative method that eliminates the need for real image labelling. For both examples, the labelling work was conducted and the results are described in the Table 5.

These quantitative outcomes prompt a discussion on what constitutes an acceptable result for the method's usage and application field. In terms of true positives, the scores on real images are relatively low, albeit encouraging, given that the network has not encountered any real infrared image during training. However, the 'large' false negative errors hold significant importance in this context. The method was not intended to serve as one of the power control factors during a discharge, but it is crucial not to overlook any PFUs. These errors could potentially lead to a misinterpretation of the resultant physical work. Indeed, it is observed that on real images (this can be confirmed on other examples not shown here), the network tends to make incorrect predictions, albeit within a perimeter of one pixel. It would be insightful to understand why this error is more prevalent on real images in order to rectify it. However, this error does not significantly impact the studies based on these results. For instance, it is still feasible to analyse the normality of the strikeline despite this error. In the context of enhancing the

first wall protection aspect of this work, it may be beneficial to consider the development of an evaluation metric that incorporates these elements. It becomes crucial to impose a more stringent penalty on 'missed' PFUs compared to those predictions that are within a one-pixel radius of the actual value. Due to these factors, establishing an acceptable threshold for TP, FN, FP, Precision, and Recall on real-time results presents a significant challenge. The emphasis may shift between these aspects based on specific requirements. From a security perspective, the preference leans towards identifying all potential hot PFUs, even if the segmentation yields multiple pixels on the same PFU. On the other hand, for the physical examination of temperature distribution along the strikeline, the ideal scenario would be the absence of false positives, ensuring a one-to-one correspondence of pixels to PFUs. Regardless, this method was not conceived to serve as a singular information source for providing control-feedback on plasma. This Constrained U-Net is integrated into a dynamic, pre-established by the detection/classification pipeline, to assist in decision-making for experts.

Nonetheless, it is deemed important to maintain the Tversky loss as a training loss function for the segmentation component of the model. This is aimed at reinforcing the objective of identifying the hottest zone/pixel within a broader hot area, an operation that could be repeated an indeterminate number of times on a single strikeline. The goal is not to learn to enumerate PFUs, but rather to pinpoint the most intense heat zone within each unit, a process that subsequently facilitates their enumeration.

The strikeline in Fig. 10 deviates from the typical pattern. This anomaly is attributed to a shock event that occurred towards the end of the experimental campaign, which led to the accumulation of a noticeable material deposit on the divertor in the strikelines' zone. The deposit, found to contain tungsten among other elements, is currently under investigation by other research team. It poses a significant challenge for infrared analysis, because it is a major perturbation to usual temperature patterns. Such perturbed temperature pattern makes it challenging for an expert human eye to differentiate between the hot zones associated with the deposit and the hot zones that result from flux deposition on the divertor.

The regression outcomes for this strikeline, while remaining within a plausible range, are less precise. The computed curvature value is a bit high, considering that the expected curvature in this region ranges between 1 and 1.5. The angle prediction is also marginally overestimated, with substantial measurement uncertainties yielding an approximate value of 12° for this strikeline. Following consultations with experts in the field, it is inferred that the conclusions derived from these angle and curvature measurements are not down to the last degree. A tolerance of approximately 10° and 0.5 curvature value may be deemed acceptable, as it does not

significantly impact subsequent physical and safety analyses. So, despite these discrepancies, the values obtained on Fig. 10 are still within acceptable limits, demonstrating a degree of robustness in the network.

In order to address the issue of potentially exaggerated predictive values, which may arise from a substantial discrepancy between simulated and real world images (like the atypical shape of the resistive deposits visible on Fig. 10), future enhancements could consider the incorporation of annotated real images into the training set. This approach may provide a more robust and realistic training environment, thereby improving the accuracy of the predictions.

Potential Application in Real Time

One of the major challenges of tokamak wall hot spot detection relies in real-time detection/identification. Fast detection is crucial as it enables the implementation of preventive measures to avoid substantial damage to the reactor. Currently, real-time detection operates with pre-programmed temperature thresholds. They serve as control mechanisms for the machine. The objective of this section is to introduce options for a real-time application of the constrained U-Net.

The temperature security server used by the institute is equipped with an NVIDIA A30 GPU, hence allowing AI model inference. It has a substantial memory capacity of 24GB, which allows it to handle complex tasks efficiently. In terms of performance, it delivers a peak FP64 performance of 5.2 TFLOPS (trillion floating-point operations per second) and a peak FP32 performance of 10.3 TFLOPS.

Given their specifications, the two optimal models (referred as A and B in Sect. 6.2) operate at an average of 170 frames per second (fps). To put this into perspective, WEST's infrared cameras capture images at a rate of 50 fps. Furthermore, the hot spot detection and classification model (detailed in [13]) is inherently a larger model compared to the one discussed in this article. Consequently, it operates inevitably below 170 fps. Therefore, the constrained U-Net is compatible with on-line usage for the real-time analysis of hot spots. This could be used to write the real time strikeline temperature on the shared memory network, playing the role of an "intelligent" ROI. Such an "intelligent" ROI has the potential of being much less sensitive to detection errors and artefacts than a prescribed and fixed ROI.

Conclusion

In recent years, strides have been made towards the automatic detection of a series of WEST divertor hot spots, known as strikelines, for safety monitoring. The usefulness of a Faster R-CNN algorithm for extracting a specific strikeline from the divertor camera's field of view has been demonstrated. But until now, strikeline detection from neural network was good but presented some false detections, all too easily discarded by human experts based on a-priori knowledge from strikeline curvature and angle. The strikeline detector was to be improved by mimicking the human expert analyse, which includes prior knowledge about strikeline pattern, expressed in the form of its curvature and angle.

This paper presents an AI algorithm dedicated to the analysis of a specific strikeline. This novel U-Net-like algorithm, without loss of generality, provides two categories of outputs: one image and two scalars, which characterize the strikelines, taking into account angle and curvature, being representative of prior knowledge.

The novelty of this work, achieved with the constrained U-Net, lies in the estimation of the location of the hotspots, regardless of their number, and the curvature and angle of the strikeline. Another innovative aspect of this work is the use of a 'Tversky' loss function to introduce some modularity in the segmentation capacities for security purpose.

On a test dataset of synthetic images, the precision, recall, and F1-Score exceed 0.98, outperforming a comparative 'classical' U-Net without regression, which yields values between 0.85 and 0.89, and an automatic max-tree based segmentation algorithm, which yields values around 0.4.

Given the results obtained on real-world acquisitions from the WEST Tokamak, there is confidence in the proposed methodology. It can easily be transposed to similar data obtained in other fusion devices such as W7-X, EAST, and later on, ITER. Results obtained on strikelines, recognized as typical hotspots by fusion specialists, are merely one facet of a larger objective. The overarching goal is to illustrate the benefits of integrating diverse forms of physical knowledge into neural networks.

Appendix A: Curvature Examples

See Fig. 11.

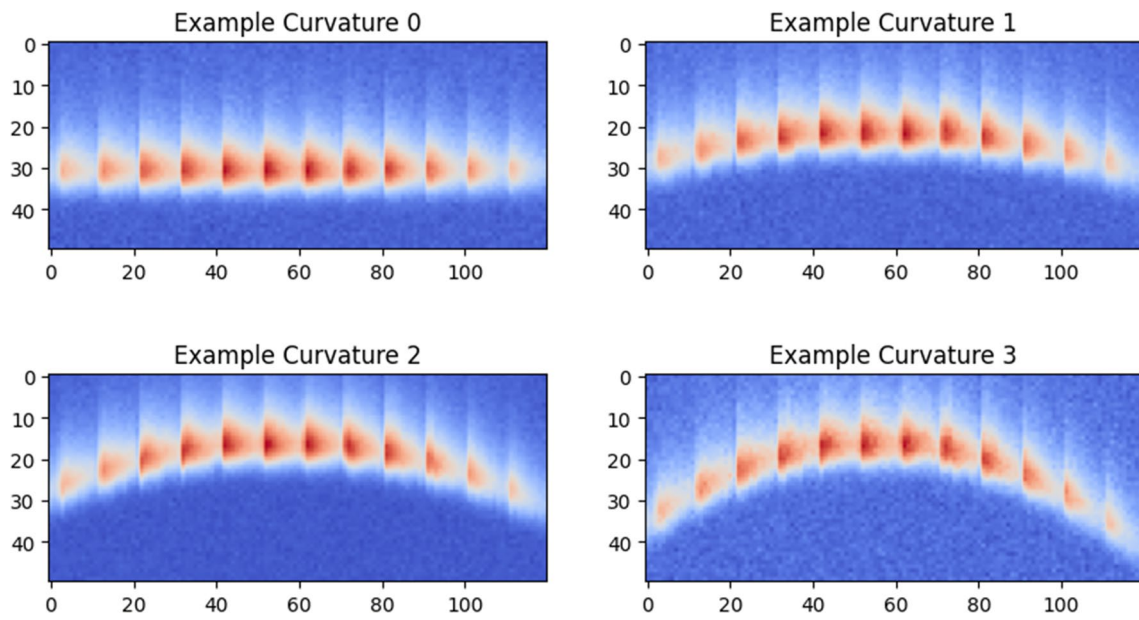


Fig. 11 Examples of the 4 possible curvatures for a 0° angular strikeline

Appendix B: Angle Examples

See Fig. 12.

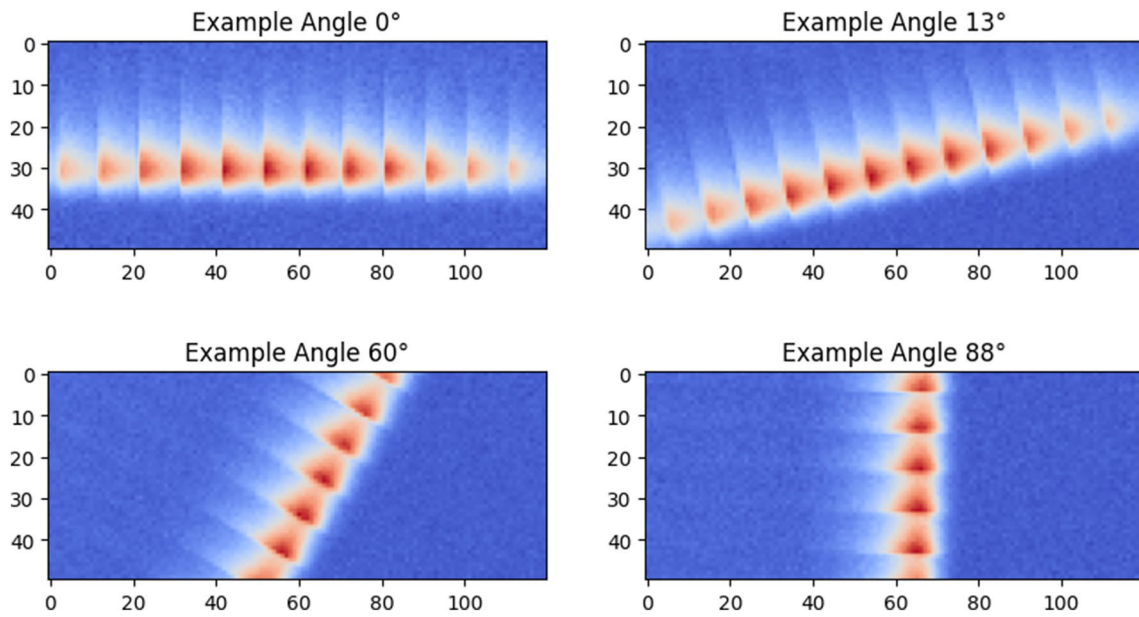
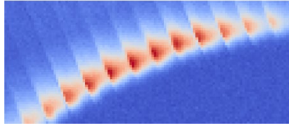

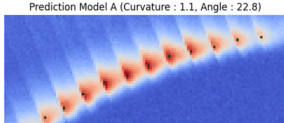
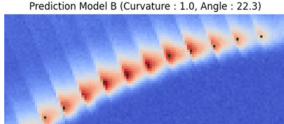
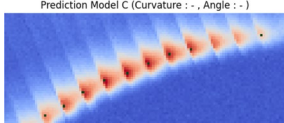
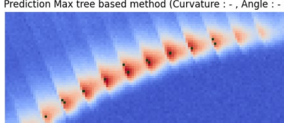


Fig. 12 Examples of 4 possible angles for a 0 curvature strikeline

Appendix C: Comparative Table of the Models

See Table 6.

Table 6 Comparative outputs table of a same input strikeline

Input image from the test dataset	Input image (test dataset) (Curvature : 1 , Angle : 23) 
Labels	Labels 
Model	Output
Model A	Prediction Model A (Curvature : 1.1, Angle : 22.8) 
Model B	Prediction Model B (Curvature : 1.0, Angle : 22.3) 
Classical U-Net	Prediction Model C (Curvature : - , Angle : -) 
Max-tree based method	Prediction Max tree based method (Curvature : - , Angle : -) 

Supplementary Information The online version contains supplementary material available at <https://doi.org/10.1007/s10894-024-00405-y>.

Acknowledgements The authors warmly thank Dr Erwan Grelier for his technical support throughout this research work. This work has been carried out within the framework of the EUROfusion Consortium, funded by the European Union via the Euratom Research and Training Programme (Grant No. 101052200 - EUROfusion). Views and opinions expressed are however those of the author(s) only and do not necessarily reflect those of the European Union or the European Commission. Neither the European Union nor the European Commission can be held responsible for them.

Author contributions V.G wrote the main manuscript, prepared the figures and did the technical work. R.M and J.M reviewed the manuscript. All authors whose names appear on the submission: - made substantial contributions to the conception or design of the work; or the acquisition, analysis, or interpretation of data; or the creation of new

software used in the work; - drafted the work or revised it critically for important intellectual content; - approved the version to be published; and - agree to be accountable for all aspects of the work in ensuring that questions related to the accuracy or integrity of any part of the work are appropriately investigated and resolved.

Data Availability The data that support the findings of this study are available on request from the corresponding author. The data are not publicly available due to privacy restriction.

Declarations

Competing interests The authors declare no competing interests.

References

- JET's final tritium experiments yield new fusion energy record (2024). <https://www.gov.uk/government/news/jets-final-tritium-experiments-yield-new-fusion-energy-record>
- ITER goals. <http://www.iter.org/sci/goals>
- J. Bucalossi, Operating a full tungsten actively cooled tokamak: overview of WEST first phase of operation. *Nuclear Fusion* **62**(4), 042007 (2022). <https://doi.org/10.1088/1741-4326/ac2525>. (Publisher: IOP Publishing)
- ...L. Wang, G.S. Xu, J.S. Hu, K.D. Li, Q.P. Yuan, J.B. Liu, F. Ding, Y.W. Yu, Z.P. Luo, J.C. Xu, L.Y. Meng, K. Wu, B. Zhang, M.W. Chen, G.Z. Deng, X.J. Liu, Z.S. Yang, X. Liu, S.C. Liu, R. Ding, G.Z. Zuo, Z. Sun, J.H. Wu, B. Cao, Y. Zhang, Y.M. Duan, L. Zhang, X.Y. Qian, A. Li, L. Chen, M.N. Jia, H. Si, T.Y. Xia, Y.W. Sun, Y.P. Chen, Q. Li, G.N. Luo, D.M. Yao, B.J. Xiao, X.Z. Gong, X.D. Zhang, B.N. Wan, H.Q. Wang, H.Y. Guo, D. Eldon, A.M. Garofalo, Y. Liang, S. Xu, C.F. Sang, D.Z. Wang, S.Y. Dai, J.Z. Sun, H.B. Ding, R. Maingi, K.F. Gan, X.L. Zou, H.L. Du, Progress of divertor heat and particle flux control in EAST for advanced steady-state operation in the last 10 years. *J. Fusion Energy* **40**(1), 3 (2021). <https://doi.org/10.1007/s10894-021-00290-9>
- G. Arnoux, S. Devaux, D. Alves, I. Balboa, C. Balorin, N. Balshaw, M. Beldishevski, P. Carvalho, M. Clever, S. Cramp, J.-L. Pablos, E. Cal, D. Falie, P. Garcia-Sanchez, R. Felton, V. Gervaise, A. Goodyear, A. Horton, S. Jachmich, A. Huber, M. Jouve, D. Kinna, U. Kruezi, A. Manzanares, V. Martin, P. McCullen, V. Moncada, K. Obreja, K. Patel, P.J. Lomas, A. Neto, F. Rimini, C. Ruset, B. Schweer, G. Sergienko, B. Sieglin, A. Soletto, M. Stamp, A. Stephen, P.D. Thomas, D.F. Valcárcel, J. Williams, J. Wilson, K.-D. Zastrow, A protection system for the JET ITER-like wall based on imaging diagnostics. *Rev. Sci. Instrum.* **83**(10), 10–727 (2012). <https://doi.org/10.1063/1.4738742>. (Publisher: American Institute of Physics)
- M.W. Chen, X.F. Yang, X.Z. Gong, K.F. Gan, B. Zhang, Z.D. Yang, Integrated infrared and visible tangential wide-angle viewing systems for surface temperature measurement and discharge monitoring in EAST. *Fusion Eng. Des.* **150**, 111415 (2020). <https://doi.org/10.1016/j.fusengdes.2019.111415>
- A. Sitjes, M. Jakubowski, A. Ali, P. Drewelow, V. Moncada, F. Pisano, T. Ngô, B. Cannas, J.-M. Traverre, G. Kocsis, T. Szepesi, T. Szabolcs, Wendelstein 7-X near real-time image diagnostic system for plasma-facing components protection. *Fusion Sci. Technol.* **74**, 1–9 (2017). <https://doi.org/10.1080/15361055.2017.1396860>
- R. Mitteau, C. Belafdil, C. Balorin, X. Courtois, V. Moncada, R. Nouailletas, B. Santraine, WEST operation with real time feed back control based on wall component temperature toward machine protection in a steady state tungsten environment. *Fusion Eng. Des.* **165**, 112223 (2021). <https://doi.org/10.1016/j.fusengdes.2020.112223>
- C.M. Bishop, P.S. Haynes, M.E.U. Smith, T.N. Todd, D.L. Trotman, Real-Time Control of a Tokamak Plasma Using Neural Networks. *Neural Comput.* **7**(1), 206–217 (1995). <https://doi.org/10.1162/neco.1995.7.1.206>
- B.D. Tracey, A. Michi, Y. Chervonyi, I. Davies, C. Paduraru, N. Lazic, F. Felici, T. Ewalds, C. Donner, C. Galperti, J. Buchli, M. Neunert, A. Huber, J. Evens, P. Kurylowicz, D.J. Mankowitz, M. Riedmiller, T.T. Team, Towards practical reinforcement learning for tokamak magnetic control. [arXiv:2307.11546](https://arxiv.org/abs/2307.11546) [physics] (2023)
- Pisano, F., Cannas, B., Fanni, A., Sias, G., Gao, Y., Jakubowski, M., Niemann, H., Sitjes, A.P., Team, W.-X, Learning control coil currents from heat-flux images using convolutional neural networks at Wendelstein 7-X. *Plasma Phys. Controlled Fusion* **63**(2), 025009 (2020). <https://doi.org/10.1088/1361-6587/abce19>
- E. Aymerich, F. Pisano, B. Cannas, G. Sias, A. Fanni, Y. Gao, D. Böckenhoff, M. Jakubowski, Physics Informed Neural Networks towards the real-time calculation of heat fluxes at W7-X. *Nuclear Materials and Energy* **34**, 101401 (2023). <https://doi.org/10.1016/j.nme.2023.101401>. (Accessed 2024-02-09)
- E. Grelier, R. Mitteau, V. Moncada, Deep learning and image processing for the automated analysis of thermal events on the first wall and divertor of fusion reactors. *Plasma Phys. Controlled Fusion* **64**(10), 104010 (2022). <https://doi.org/10.1088/1361-6587/ac9015>. (Publisher: IOP Publishing)
- X. Courtois, M. Aumeunier, C. Balorin, J.B. Migozzi, M. Houry, K. Blanckaert, Y. Moudden, C. Pocheau, A. Saille, E. Hugot, M. Marcos, S. Vives, Full coverage infrared thermography diagnostic for WEST machine protection. *Fusion Eng. Des.* **146**, 2015–2020 (2019). <https://doi.org/10.1016/j.fusengdes.2019.03.090>
- V. Martin, G. Dunand, V. Moncada, M. Jouve, J.-M. Traverre, New field programmable gate array-based image-oriented acquisition and real-time processing applied to plasma facing component thermal monitoring. *Rev. Sci. Instrum.* **81**(10), 10–113 (2010). <https://doi.org/10.1063/1.3475787>. (Publisher: American Institute of Physics)
- E. Grelier, R. Mitteau, V. Moncada, Deep learning-based process for the automatic detection, tracking, and classification of thermal events on the in-vessel components of fusion reactors. *Fusion Eng. Des.* **192**, 113636 (2023). <https://doi.org/10.1016/j.fusengdes.2023.113636>
- O. Ronneberger, P. Fischer, T. Brox, U-Net: convolutional Networks for Biomedical Image Segmentation. [arXiv:1505.04597](https://arxiv.org/abs/1505.04597) [cs] (2015)
- N. Siddique, S. Paheding, C.P. Elkin, V. Devabhaktuni, U-Net and its variants for medical image segmentation: a review of theory and applications. *IEEE Access* **9**, 82031–82057 (2021). <https://doi.org/10.1109/ACCESS.2021.3086020>. (Conference Name: IEEE Access)
- R. Azad, E.K. Aghdam, A. Rauland, Y. Jia, A.H. Avval, A. Bozorgpour, S. Karimijafarbigloo, J.P. Cohen, E. Adeli, D. Merhof, Medical image segmentation review: the success of U-Net. [arXiv:2211.14830](https://arxiv.org/abs/2211.14830) [cs, eess] (2022)
- A. Juven, M.-H. Aumeunier, R. Brunet, M.L. Bohec, M. Adel, R. Miorelli, X. Artusi, C. Reboud, Temperature estimation in fusion devices using machine learning techniques on infrared specular synthetic data. In: 2022 IEEE 14th image, video, and multidimensional signal processing workshop (IVMSP), pp. 1–5 (2022). <https://doi.org/10.1109/IVMSP54334.2022.9816270>
- A. Kos, An u-net-based regression model incorporating a parametric description of the prostate
- V. Gorse, R. Mitteau, J. Marot, Anomaly classification by inserting prior knowledge into a max-tree based method for divertor hot spot characterization on WEST tokamak. *Rev. Sci. Instrum.* **94**(8), 083510 (2023). <https://doi.org/10.1063/5.0156956>
- Homepage | Cast3M <http://www-cast3m.cea.fr/index.php>
- Eich, T., Leonard, A.W., Pitts, R.A., Fundamenski, W., Goldston, R.J., Gray, T.K., Herrmann, A., Kirk, A., Kallenbach, A., Kardaun, O., Kukushkin, A.S., LaBombard, B., Maingi, R., Makowski, M.A., Scarabosio, A., Sieglin, B., Terry, J., Thornton, A., ASDEX Upgrade Team, JET EFDA contributors: scaling of the tokamak near the scrape-off layer h-mode power width and implications for ITER. *Nucl. Fusion* **53**(9), 093031 (2013). <https://doi.org/10.1088/0029-5515/53/9/093031>
- M. Firdaouss, V. Riccardo, V. Martin, G. Arnoux, C. Reux, Modelling of power deposition on the JET ITER like wall using the code PFCFLux. *J. Nucl. Mater.* **438**, 536–539 (2013). <https://doi.org/10.1016/j.jnucmat.2013.01.111>

26. S.S.M. Salehi, D. Erdogmus, A. Gholipour, Tversky loss function for image segmentation using 3D fully convolutional deep networks. [arXiv:1706.05721](https://arxiv.org/abs/1706.05721) [cs] (2017)
27. H. Gabor, The Tversky loss function and its modifications for medical image segmentation
28. P. Salembier, A. Oliveras, L. Garrido, Antiextensive connected operators for image and sequence processing. *IEEE Trans. Image Process.: A Publ. IEEE Signal Process. Soci.* **7**, 555–70 (1998). <https://doi.org/10.1109/83.663500>

Publisher's Note Springer Nature remains neutral with regard to jurisdictional claims in published maps and institutional affiliations.

Springer Nature or its licensor (e.g. a society or other partner) holds exclusive rights to this article under a publishing agreement with the author(s) or other rightsholder(s); author self-archiving of the accepted manuscript version of this article is solely governed by the terms of such publishing agreement and applicable law.